Analysis of a hyperprism for exciting high-*k* modes and subdiffraction imaging

Md. Samiul Habib,[1,2,*] Alessio Stefani,[1,3] Shaghik Atakaramians,[1,4] Simon C. Fleming,[1] and Boris T. Kuhlmey[1,†]
[1]*The University of Sydney, School of Physics, Institute of Photonics and Optical Science, Camperdown, New South Wales 2006, Australia*
[2]*Department of Electrical & Electronic Engineering, Rajshahi University of Engineering & Technology, Rajshahi 6204, Bangladesh*
[3]*DTU Fotonik, Department of Photonics Engineering, Technical University of Denmark, DK-2800 Kongens Lyngby, Denmark*
[4]*School of Electrical Engineering and Telecommunications, The University of New South Wales, Sydney, New South Wales 2052, Australia*

(Received 12 April 2018; revised manuscript received 5 September 2019; published 19 September 2019)

We study the effect of resonances on the ability of prisms made of hyperbolic metamaterials in the canalization regime (such as wire array media) to couple evanescent high spatial frequencies (high-*k* modes) to low spatial frequencies that propagate in the far-field zone. Using simple analytical models, we calculate the far-field propagation from the hyperprism. The resonant nature of the metal wire segments within the prism yields a transmission function identical to that of a grating, but with periodicity proportional to the wavelength, making the hyperprism function like a *nondispersive grating*. Numerically compensating the effect of resonances allows the hyperprism to be used as a one-dimensional imaging device able to resolve feature sizes below the diffraction limit if the host medium has a low refractive index. Furthermore, the hyperprism enables coupling of propagating plane waves to a range of high-*k* modes that can be increased by increasing the angle of the prism. We quantify how this tunable, nondispersive excitation of high-*k* modes opens up possibilities for new experimental approaches for coupling to plasmonic systems and for increased axial resolution in total internal reflection imaging, in particular in the terahertz spectrum.

DOI: 10.1103/PhysRevB.100.115146

I. INTRODUCTION

Metamaterials [1] are engineered subwavelength composite materials that allow unprecedented control of the electromagnetic response, leading to a new class of exciting phenomena not attainable with conventional materials. Among various metamaterials explored to date, hyperbolic metamaterials (HMMs) have received widespread attention in the scientific community due to their structural simplicity and the variety of important applications spanning the frequency range from microwave to ultraviolet [2]. A HMM is a highly anisotropic artificial medium, in which the real parts of different electric (or magnetic) response tensor components have different signs, resulting in an open hyperbolic dispersion profile [3,4]. The hyperbolic dispersion profile can be achieved using alternating subwavelength layers of metal and dielectric (layered media) [5] or by distributing subwavelength parallel metallic wires in a dielectric host (wire media) [6]. Idealized HMMs have the unique property of supporting propagating waves with arbitrary high-*k* vectors, which would be evanescent in conventional dielectrics [3]. Owing to the unbounded dispersion profile, HMMs offer a large range of potential applications such as negative refraction [7,8], spontaneous emission and radiation enhancement [9–12], optical analogs for cosmology [13,14], and nanoscale light confinement [15,16].

One of the most promising applications of high-*k* modes in HMMs is to create diffraction-beating devices such as hyperlenses [17,18]. A properly designed HMM device can couple high-*k* modes to low spatial frequencies propagating in free space, allowing magnification of subwavelength objects [17]. Conversely, hyperlenses can be used to couple free-space propagating waves to high-*k* waves such as surface waves [19]. While this is not the only way to couple to high-*k* waves (alternatives being high-index prisms [20–22], gratings [23,24], and simple sharp objects), hyperlenses offer additional versatility, for example, for focusing below the diffraction limit [25], and could provide access to a wider range of spatial frequencies.

Most experimental realizations of magnifying hyperlenses relied on curved geometries [17,18,26] or tapering of the structure [27–29]. Hyperlenses based on wire media have been fabricated at various frequency ranges, including microwave [28], terahertz (THz) [29], and midinfrared [30]. At microwave frequencies, early imaging experiments were performed using manually assembled slabs and tapered wire media [28,31]. Imaging experiments at THz frequencies using fiber-based hyperlenses demonstrated resolution down to $\lambda/28$ [29]. However, such hyperlenses are difficult to produce, especially in large numbers [29], because of their shape.

An alternative structure offering some of the functionality of hyperlenses is that of a HMM prism geometry, first suggested by Salandrino and Engheta [18]. The use of hyperprisms of various shapes to convert high-*k* to low-*k* waves was studied by Valagiannopoulos *et al.* to increase dipole emission to free space [10], but otherwise, the prism geometry has not received much attention. In many cases it is a much easier geometry to produce. A hyperprism can couple propagating waves on the slanted side to high-*k* waves at its base, in a way similar to a simple dielectric prism. This can be used to excite surface waves, but conversely, it can be used to magnify

*Corresponding author: samiul.engieee@gmail.com
†boris.kuhlmey@sydney.edu.au

subdiffraction features in the near-field zone of the base, in only one dimension, and thus also has potential for imaging. It appears that, conceptually, the limitation to one-dimensional imaging could be overcome by a conical geometry, where a wire array fiber could be sharpened like a pencil and thus relatively easy to make. Each radial section of the cone would act as a prism, justifying the study of the prism as a potential imaging device.

We recently fabricated and experimentally characterized a wire array prism at THz frequencies, showing the resolution of features below the diffraction limit with a twofold magnification along one dimension in the near-field zone [32]. However, a prism is not as convenient as a lens for imaging: while we demonstrated magnification in the near-field zone, the phase of the information is heavily affected by multiple resonances within the prism, scrambling the far-field images. It is thus not clear how and whether such a simple prism of HMM (or hyperprism) can indeed couple high-k modes to far-field propagating plane waves.

In this paper, we explore the consequence of the hyperprism's resonances, both for subdiffraction imaging and for exciting high-k modes from the far-field zone. We use the specific example of a hyperprism used in previous experimental studies [32], with the geometry described in Sec. II. Using homogenization of wire array metamaterials and a Fabry-Pérot resonator model, we devise a simple transfer function of the hyperprism (Sec. III), allowing us to calculate how well subdiffraction spatial features are preserved in the far-field field distribution and the limit of high-k values that can be coupled to from free space (Sec. IV). Taking into account wire resonances, the transfer function is, in essence, that of a grating: in Sec. V we analyze the resulting grating effects and show that the effective period of the grating is proportional to the wavelength so that the hyperprism acts as a nondispersive grating. In Sec. VI, we show that even in the presence of the inevitable resonances, the high-k modes can, in principle, be used for subdiffraction imaging if the effect of resonances is compensated for and investigate the imaging performance of the hyperprism. In Sec. VII we quantify the potential of hyperprisms for exciting graphene THz plasmons and for total internal reflection microscopy, where the reduced penetration depth could lead to $\lambda/100$ longitudinal resolution. Finally, in Sec. VIII we validate our simple analytic model with full vector numerical simulations before concluding.

II. GEOMETRY

A two-dimensional (2D) schematic of the wire array hyperprism under consideration is shown in Fig. 1(b). The hyperprism is simply a section of a wire array embedded in a dielectric of refractive index n [light blue region in Fig. 1(b)], with one section perpendicular to the wire (the base) and the other section at an angle θ to the first. In the canalization regime [33] fields propagate purely parallel to the wires. This means fields due to a source on the base end up projected on the larger slanted section, with the projection yielding magnification by a factor $M = 1/\cos(\theta)$. Our analytic study relies on the homogenized canalization behavior and does not depend on wire spacing, which thus remains undefined (or assumed to be infinitely small). Because hyperlenses are

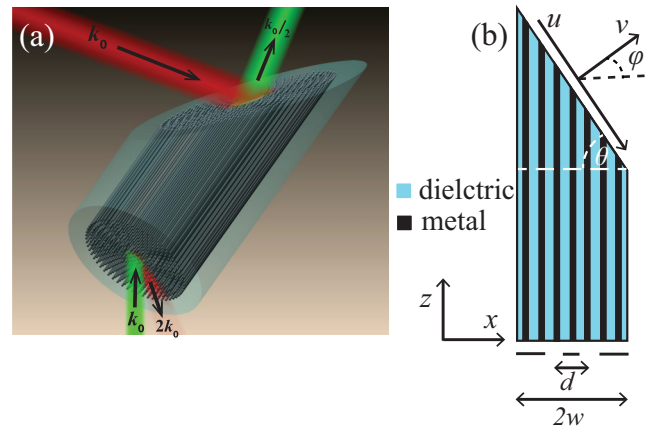

FIG. 1. Schematic of the wire array hyperprism. (a) The principle of subdiffraction imaging and surface plasmon excitation are shown in green and red. (b) Two-dimensional representation of the hyperprism with a two-slit object, where d, $2w$, θ, and φ represent the center-to-center distance between slits, prism width, prism angle, and angle of refraction, respectively.

typically small, of sizes comparable to the wavelengths, their finite size must be taken into account. In all examples studied in this paper we use the following design, which can be scaled to any wavelength. We chose $\theta = 60°$ so that the magnification is 2 and a width of the prism base $2w$ that is 3/5 of the shortest wire. Figure 1(b) also shows a double slit that will be used to characterize the imaging performance of the prism. The center-to-center distance between slits d represents the scale of features to be resolved. We calculate the distribution of fields in the far-field zone, an amplitude function of the refraction angle φ for any given object at the input face of the prism. We expect that each spatial frequency k_x at the object plane can be mapped to an angle of refraction φ.

III. THEORETICAL FRAMEWORK

We begin our analytical treatment by considering the medium to be homogeneous, but in the canalization regime, meaning fields propagate only in the direction of the wires, i.e., along z. We consider the problem to be two-dimensional and consider only the extraordinary waves [2], which can thus be described by their scalar amplitude. In such a case, the output field $E_o(u)$ along the slanted side of the prism depends only on the input field $E_i(x)$ at the same value of $x = u\cos(\theta)$, where θ is the prism angle. The output field can be expressed by

$$E_0(u, f) = E_i(x, f)T(x, f), \tag{1}$$

where f is the frequency and $T(x, f)$ denotes the local transfer function of the prism. In this first model, we neglect losses and the effect of wire resonances. The phase accumulated in the prism is then simply proportional to the wire length and thus proportional to x and the slope of the interface, leading to a phase ramp as a function of x. The local transfer function of the prism with finite width $2w$ can then be written as

$$T(x, f) = \Pi(x/w)e^{(ik_z sx)}, \tag{2}$$

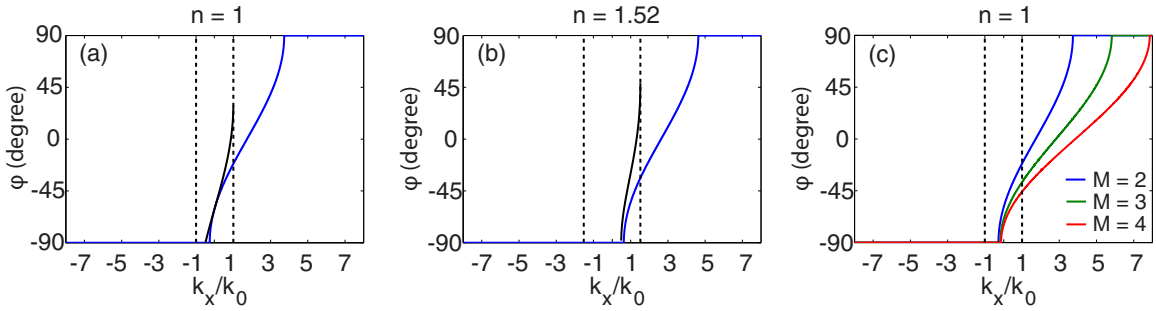

FIG. 2. Mapping of input spatial frequencies k_x/k_0 to angle of refraction φ for (a) $n = 1$ and (b) $n = 1.52$. Mapping is evaluated for $w \to \infty$. The blue and black curves represent mapping for the hyperprism and a plain isotropic prism, respectively. (c) Mapping of input spatial frequencies k_x/k_0 to angle of refraction φ, for $n = 1$ with two-, three-, and fourfold magnifications.

where $s = -\tan(\theta)$ is the slope of the interface, k_z is the wave-vector component in the direction of the wires, and Π is the rectangular function. In the canalization regime, the wave vector becomes $k_z = nk_0$, where k_0 is the free-space wave number and n is the refractive index of the dielectric host.

The output field given by Eq. (1) is at the interface, that is, in the near-field zone. However, we are interested in investigating far-field propagation away from the prism because hyperlenses are most useful if the images are reconstructed in the far field. To investigate how the spatial features are kept in the far-field distribution, we consider the output field in the spatial Fourier domain, which can be obtained by applying the Fourier transform to Eq. (1):

$$\tilde{E}_0(k_u, f) = \tilde{E}_i(k_x, f) * \tilde{T}(k_x, f), \tag{3}$$

where the output field in Fourier space is given by the convolution of the input field $\tilde{E}_i(k_x, f)$ and the transfer kernel $\tilde{T}(k_x, f)$, where the convolution product * is a convolution on k_x and is calculated at $k_x = k_u/\cos(\theta)$. We evaluate the transfer kernel by applying the Fourier transform to Eq. (2):

$$\tilde{T}(k_x, f) = 2w\,\mathrm{sinc}(wnk_0 s + wk_x). \tag{4}$$

This shows that the spatial frequencies are shifted and spread. The spreading arises from diffraction through the finite width of the prism, and the shifting of the spatial frequencies depends on the refractive index and slope of the interface. Asymptotically, for a large prism width $w \to \infty$ the transfer kernel of Eq. (4) becomes a Dirac delta function:

$$\tilde{T}(k_x, f) = \delta(nk_0 s + k_x). \tag{5}$$

Equation (5) suggests a simple mapping from input spatial frequencies, k_x to k_u (spatial frequencies at the output interface), so that

$$k_u = k_x \cos(\theta) + k_z s \cos(\theta). \tag{6}$$

This incorporates the magnification since the spatial frequencies are reduced by $\cos(\theta)$ and a shift in spatial frequencies, corresponding to the rotation of the coordinate system (x to u) and to refraction.

IV. ANALYSIS OF FAR-FIELD PROPAGATION

A. Limit of infinite width

To investigate how input spatial frequencies propagate to the far field, we plot the angle of refraction, $\varphi = \sin^{-1}(k_u/k_0)$ as a function of input spatial frequency k_x based on the simple bijective map for infinite width resulting from Eq. (6). A nonpropagating solution will be obtained when $k_u > k_0$, which implies the refraction angle will be complex with a real part of $\pm 90^\circ$, indicating the waves will be reflected back into the hyperprism.

Figures 2(a) and 2(b) present the mapping of input spatial frequencies for the hyperprism (blue curve) and a prism consisting of an isotropic material with the same refractive index (black curve) for comparison. The mapping is evaluated by considering the wires in air [$n = 1$; Fig. 2(a)] and in a medium with $n = 1.52$ [Fig. 2(b)] for twofold magnification ($\theta = 60^\circ$). The vertical dotted lines in Figs. 2(a) and 2(b) show spatial frequencies corresponding to the diffraction limit in the dielectric. For the isotropic plain prism, φ can be obtained simply from Snell's law. To get a better understanding of these diagrams, we consider the case of waves with $k_x = 0$, corresponding to waves with phase propagating purely along z in the medium. For Fig. 2(a), the black curve corresponds to an isotropic "air prism" in air, that is, propagation in free space. For the isotropic air prism, at $k_x = 0$ the angle of propagation is $\varphi = -60^\circ$ simply because φ is in a rotated reference frame (no refraction is taking place). For the isotropic prism with refractive index $n = 1.52$, φ is different from $-\theta$ at $k_x = 0$, indicating refraction (or, in this case, total internal reflection) is taking place [Fig. 2(b)]. For both isotropic prisms the input spatial frequencies k_x coupling to propagating output waves are restricted by the diffraction limit, as expected.

In contrast, the hyperprism carries waves with large k_x that can still couple to propagating waves in air at the interface and thus enables the mapping of far-field propagating waves to spatial frequencies beyond the diffraction limit. The minimum and maximum accessible k_x can be found directly from $k_x/k_0 = \mp M + n\sqrt{M^2 - 1}$, where M is the magnification factor. This can be interpreted in two ways: high-k information at the bottom facet of the prism will couple to propagating waves in the far field, which can be used for subdiffraction imaging from the far-field zone, or conversely, a far-field beam

incident on the upper angled facet can be efficiently coupled to high-k waves at the prism's lower surface, for example, to excite surface plasmon polaritons. Compared to air, for $n = 1.52$ the hyperprism allows mapping of a wider range of spatial frequencies [see Fig. 2(b)]. From the mapping for the hyperprism it can be seen that below a certain k_x value the real part of the refraction angle is -90°, meaning light cannot exit the output interface and is instead reflected back into the hyperprism.

One of the advantages of the hyperprism is that the range of accessible k vectors can simply be increased by increasing the slope of the prism (thus enhancing magnification), as shown in Fig. 2(c) for $n = 1$. The magnification of the hyperprism is changed by varying the prism angle θ, and we chose prism angles 60°, 70.5°, and 75.5°, corresponding to two-, three-, and fourfold magnifications, respectively. Thus the hyperprism enables excitation of very high k modes even with air as the host medium, which could avoid the requirement of high-refractive-index materials to excite surface plasmon polaritons (SPPs) in the prism coupling technique.

B. Finite-width effects

For the same finite width as mentioned earlier and magnification of 2, the amplitude of the output fields $\tilde{E}_0(\varphi)$ for an input harmonic field with a single spatial frequency is calculated using Eqs. (3) and (4). The resulting mapping shown in Figs. 3(a) and 3(b) for $n = 1$ and $n = 1.52$, respectively, matches the shape of Figs. 2(a) and 2(b), but with additional diffraction due to the finite width of the prism. Similar to results in Fig. 2(b), larger n provides a wider range of spatial frequencies accessible from the far-field zone [see Fig. 3(b)].

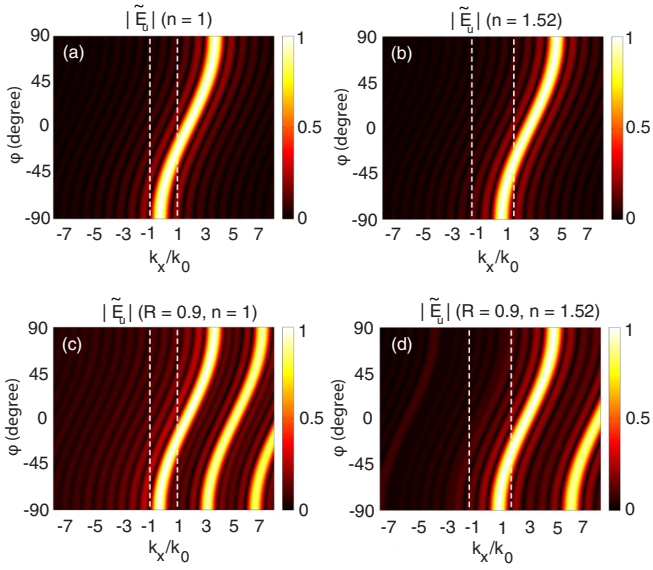

FIG. 3. Normalized amplitude of the output field as a function of input spatial frequencies and angle of refraction for (a) and (b) the nonresonant and (c) and (d) resonant cases. The mapping is evaluated for $n = 1$ (left column) and $n = 1.52$ (right column).

C. Effect of wire resonances

The homogenized, nonresonant model used above shows the basic physics of how spatial frequencies propagate to the far-field zone. However, this model is fundamentally incomplete since it ignores wire resonances. Resonances greatly affect the phase and amplitude of the transmitted field and thus the far-field pattern. Since each wire has different resonant frequencies, it is not obvious how this will impact the far-field pattern. To improve our analytical model, we now use a more realistic approach based on Fabry-Pérot resonators to account for wire resonances.

In this model, we treat each of the wire segments as Fabry-Pérot cavity resonators, and the transfer function for a single wire can be written as [34]

$$T_{\mathrm{FP}}(x, f) = e^{i\delta/2}[(1 - R)/(1 - Re^{i\delta})], \tag{7}$$

where $\delta = 2k_z nL(x)$ is the phase for one round trip along the wire length $L(x)$ and R is the reflectivity at both interfaces. For a fixed frequency, the local transfer function T_{FP} is periodic in δ and thus in x: the effect of the resonances is akin to multiplying the resonance-free transfer function by a grating-like transfer function. From this simple realization, we can expect that this resonant model will yield a far-field pattern similar to that of the nonresonant model, but with additional diffraction lobes. For the same geometry and dielectrics as in Figs. 3(a) and 3(b), the output field profile for $R = 0.9$ is shown in Figs. 3(c) and 3(d). Additional diffraction lobes are indeed found for large spatial frequencies. The additional diffraction lobes are shifted for a larger refractive index [see Fig. 3(d)], and their intensity depends on the reflectivity, R.

V. ANALYSIS OF EFFECTIVE GRATING EFFECTS

The location of the additional sidelobes can be determined based on the effective grating's periodicity using the usual grating equation [35]:

$$k_u = k_{u0} + m\left(\frac{2\pi}{\Lambda}\right), \tag{8}$$

where m and Λ are the grating order and period, k_u is the wave vector of diffracted orders at the interface, and $k_{u0} = k_x\cos(\theta) + k_z s\cos(\theta)$ is the projected wave vector at the interface. From the phase of the transfer function T_{FP} and from Eq. (7), the effective grating period is

$$\Lambda = \frac{\lambda}{2ns}, \tag{9}$$

where λ is the vacuum wavelength and s is the slope of the prism. From Eq. (9) the grating period is independent of the overall length of the prism and depends on only the refractive index, prism slope, and, intriguingly, the wavelength of light. The input spatial frequencies mapped to the angle of refraction for different grating orders are illustrated in Figs. 4(a) and 4(b) for $n = 1$ and $n = 1.52$. The red curves for both plots show the mapping for $m = 0$, which is clearly matched to that of the central field distribution shown in Figs. 3(c) and 3(d), whereas the additional diffraction lobes in Figs. 3(c) and 3(d) are matched for negative grating orders. Equation (9) implies that, remarkably, owing to the appearance of the grating as a result of resonances, the period of the effective

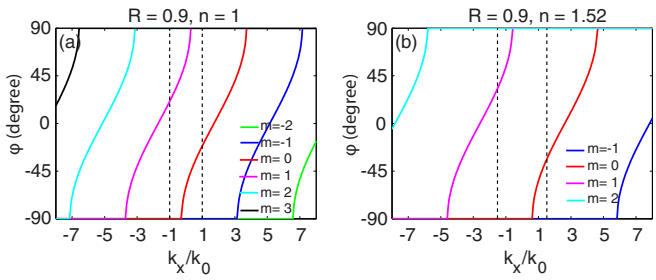

FIG. 4. Mapping of input spatial frequencies to the angle of refraction for (a) $n = 1$ and (b) $n = 1.52$. The mapping is evaluated for $w \to \infty$ and calculated for different grating orders.

grating is proportional to the wavelength λ. As a consequence, Eq. (8) can also be written as $k_u/k_0 = k_{u0}/k_0 + 2mns$. Given $\sin^{-1}(k_u/k_0)$ gives the angle of diffraction of order m, we see that for a fixed input angle, the angle of the diffraction orders is *independent* of the wavelength, making the device a *nondispersive grating*—in the limit that the background material's dispersion can be ignored, which is ostensibly the case if $n = 1$.

VI. FAR-FIELD IMAGE RECONSTRUCTION

For a nonresonant, infinitely large hyperprism, there is a bijective map between the far-field direction and spatial frequency (Fig. 2), so that recording the far-field should enable imaging with the extended spatial frequency range provided by the hyperprism. However, for finite, resonant hyperprisms the mapping between angle and spatial frequency is not unique. To analyze the imaging performance of the hyperprism, we consider an object consisting of two subwavelength slits with slit width $a = (2/3)d$, where d is the center-to-center distance between slits. To reconstruct the image of subwavelength objects in the far-field zone, the following steps have been taken. First, we calculate the output field $E_0(u)$ at the output interface, which can be given by multiplying the input field $E_i(x)$ by the local transfer function T_{FP}, thus providing the output field in the near-field zone (at the interface). We take the Fourier transform of this output field, giving the far-field distribution as a function of the refraction angle φ. We then map the far-field information back to near-field information of the object, expressed in the spatial frequency domain using Eq. (6), as shown in Fig. 5(a). Finally, to regain the output field in real space we apply the inverse Fourier transform.

The calculated intensity profile after image reconstruction is shown in Figs. 5(b) and 5(c). We evaluate the intensity profile for resonant and nonresonant cases, considering a dielectric host with refractive index $n = 1$. Figure 5(b) shows the intensity profile for the nonresonant case, and Fig. 5(c) shows that for the resonant case with reflectivity $R = 0.9$. For both cases the intensity profile is evaluated at a fixed normalized wavelength, $\lambda/d = 2.5$. At this wavelength the size and separation of the slits are below the diffraction limit. For the nonresonant case and $n = 1$, it can be seen that the reconstructed image clearly resolves the individual slits, shown in Fig. 5(b). In this case image reconstruction is possible because the hyperprism is able to map high spatial frequencies, including the zero spatial frequency $k_x = 0$ [Fig. 5(a)]. For the resonant case with $R = 0.9$, the intensity of one of the imaged slits drops by ∼40% [Fig. 5(c)]. The intensity reduction for the resonant case strongly depends on the wavelength. To show this, we now present the images as a function of wavelength and position, which we refer to as a line scan [36].

The reconstructed intensity line-scan profiles for the resonant and nonresonant cases are shown in Fig. 6. For the nonresonant case with $n = 1$, the hyperprism is capable of resolving the subdiffraction features over a broad spectral range, as shown in Fig. 6(a). However, for the same refractive index but with $R = 0.9$, there is significant image distortion [Fig. 6(b)]. The image distortion is due to the different resonance frequencies of different wires. As a result, in contrast to parallel slab wire media, there is no single optimal imaging frequency for the hyperprism. To eliminate the resonances of the individual wires, we use a space-dependent convolution technique [32] previously described for use in the near-field zone, but now using the far-field data. The intensity after the convolution is plotted in Fig. 6(c), showing significant improvement of the image over a broad spectral range.

We now investigate imaging performance of the hyperprism if $n = 1.52$. As before, we calculate the wavelength-dependent intensity profile for $R = 0$ and $R = 0.9$. In this case the hyperprism cannot resolve the subdiffraction features [Fig. 6(d)]. This phenomenon can be explained by the fact that all negative spatial frequencies, including the zero spatial frequency, are lost for $n = 1.52$ [Figs. 2(b) and 3(b)], implying

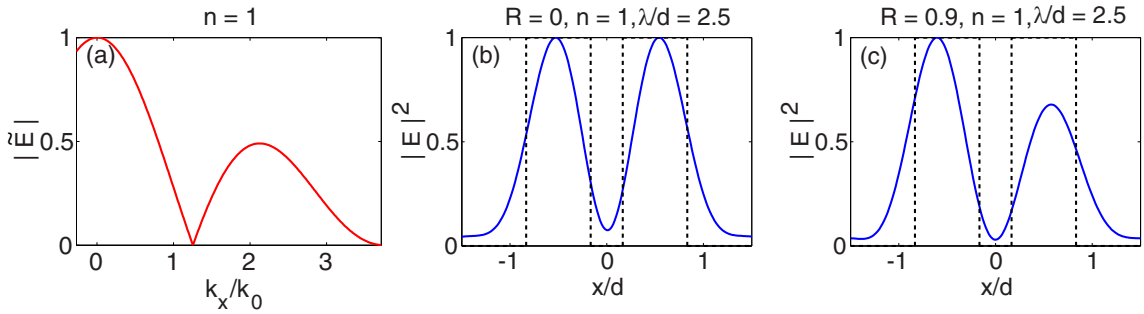

FIG. 5. (a) Normalized amplitude of the output field as a function of input spatial frequencies. Reconstructed intensity profile for (b) $R = 0$ and (c) $R = 0.9$. The intensity profile is evaluated for $n = 1$. Dashed lines indicate the size and separation of the slits.

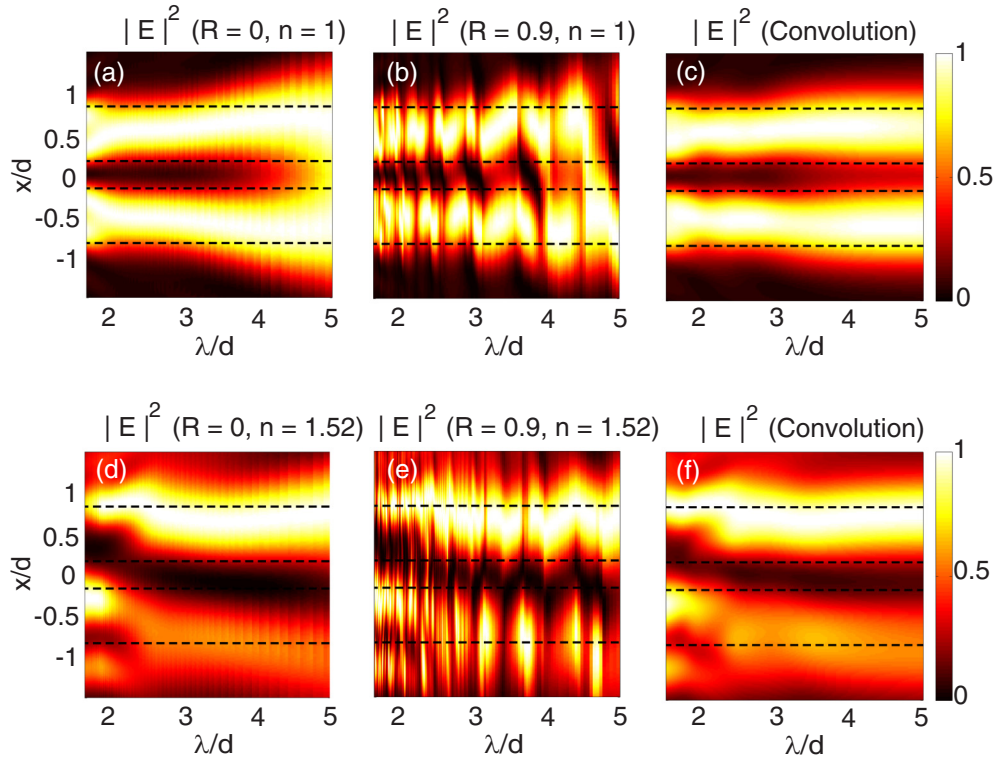

FIG. 6. Calculated wavelength-dependent intensity profile (a) and (d) for $R = 0$, (b) and (e) for $R = 0.9$, and (c) and (f) after convolution. The intensity is evaluated for $n = 1$ (top row) and $n = 1.52$ (bottom row). Horizontal dashed lines indicate the size and separation of the slits.

loss of phase and low spatial frequency information. As a consequence, it is impossible to reconstruct the image with any fidelity. The images are further degraded for the resonant case [Fig. 6(e)]. The intensity profile after convolution for the resonant case is shown in Fig. 6(f): the wavelength-dependent artifacts have been mitigated, but the image still suffers from the loss of low spatial frequencies. How resonant a prism is strongly depends on the spectrum of interest, material losses, and density of wires. In an example studied in Sec. VIII we found $R \simeq 0.2$, making resonance effects relatively weak.

VII. APPLICATIONS OF HIGH-k MODE EXCITATION

In the previous sections we have shown that the hyperprism can be used to magnify subdiffraction features for far-field imaging. However, it allows only one-dimensional magnification and is further limited when the host index is not small due to the loss of negative spatial frequencies. In many ways this is not entirely surprising, as dielectric prisms are known as dispersive tools for exciting surface plasmons [20] or for frustrated total internal reflection tomography [37], more so than they are for imaging. Here we explore whether hyperprism applications mimicking a conventional prism, tunably coupling free-space plane waves to high-k modes, are more promising. The hyperprism's advantage is, of course, the wider range of accessible k. This is of particular benefit for surface plasmon excitation and total internal reflection microscopy. We center our discussion on applications in the THz spectrum, where hyperprisms are relatively easy to make.

A. THz graphene plasmons

Graphene can support SPPs at relatively low frequencies, including the far infrared and THz, with properties adjustable through doping and applied gate voltage [38–40]. Depending on the latter, graphene SPPs can propagate over several wavelengths above 3 THz or can instead be strongly absorbed and be used to modulate THz radiation, also at lower THz frequencies [41–43]. To couple efficiently to the plasmon, phase matching is required, which can be achieved using gratings or prisms. Gratings are highly dispersive and typically provide narrow-band coupling, while prisms can couple to SPPs only with an effective index lower than the prism's refractive index. In contrast, a hyperprism could provide wideband coupling over an extended range of effective indices matching k_x/k_0 in Fig. 2. Figure 7 shows the effective index of SPPs of a single layer of graphene on a dielectric substrate with $n = 1.52$ (for consistency with the background index used in hyperprism simulations), calculated using dispersion relations and data from Ref. [39]. SPPs with an effective index above 1.52 cannot be coupled to using a simple dielectric prism with the same refractive index, but a prism with $M = 4$ could couple SPPs with effective indices in excess of 7, over a broad spectrum, widening the range of frequencies and bias voltage over which graphene-based SPP modulators could be used [43].

B. Total internal reflection microscopy and tomography

In total internal reflection microscopy, a low-refractive-index sample is positioned on a high-index lens or prism and illuminated from the high-index side at angles at which total

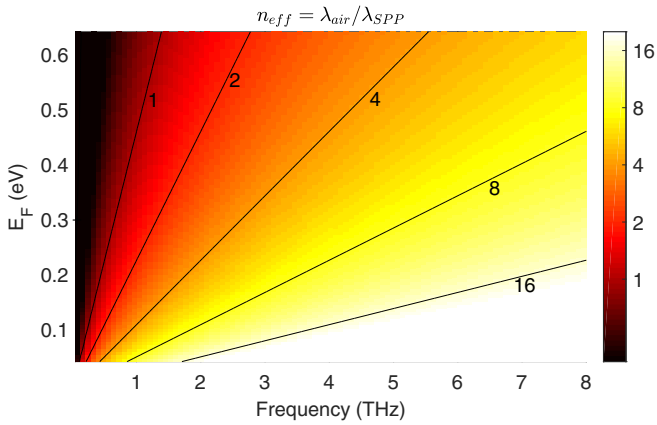

FIG. 7. Effective index of surface plasmon polaritons of a single layer of graphene between air and a refractive index of $n = 1.52$ as a function of Fermi energy E_F and frequency.

internal reflection occurs. The sample is thus illuminated by only the evanescent field, which can allow for high longitudinal resolution. By scanning the angle of incidence and thus the penetration depth, a three-dimensional image with subwavelength longitudinal resolution can be reconstructed [37,44]. Total internal reflection microscopy is particularly useful to image within highly absorbing samples, for example, in water at THz frequencies [45].

The use of a hyperprism enables coupling to evanescent fields with a penetration depth far shallower than possible using simple dielectric prisms. The penetration depth can be defined by the $1/e$ decay length of intensity in a sample of refractive index n_s:

$$d_p = \frac{1}{2\sqrt{k_x^2 - n_s^2 k_0^2}}. \tag{10}$$

Figure 8 shows d_p in air ($n_s = 1$) as a function of the angle of incidence φ at 1THz for hyperprisms with various magnification ratios M (background index $n = 1.52$), using the nonresonant mapping of φ to k_x resulting from Eq. (6). The

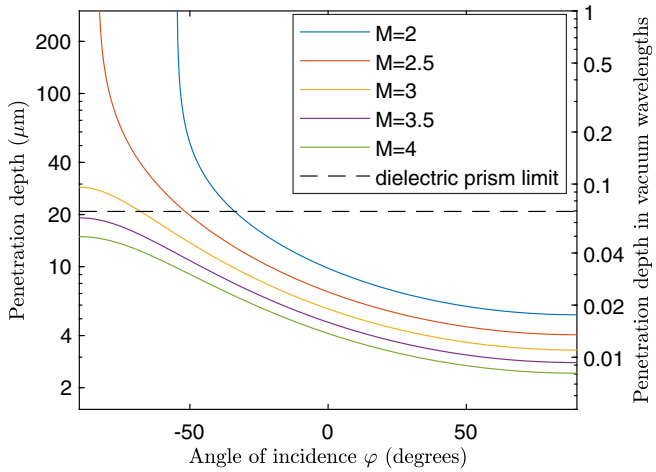

FIG. 8. Intensity $1/e$ penetration depth in air as a function of the angle of incidence for a hyperprism with $n = 1.52$ at $f = 1$ THz.

dashed line indicates the limit of penetration depth possible with a simple dielectric prism with the same refractive index 1.52. Penetration depths lower than $\lambda/100$ can be achieved with $M = 4$, greatly exceeding the limit of penetration depth of simple dielectric prisms. At large angles of incidence and thus large k_x, $d_p \sim 1/(2k_x)$ and only weakly depends on sample index n_s, so the penetration depths in the high-angle part of Fig. 8 are indicative of that for vast a range of samples. For example, for $M = 4$ in water at 1THz ($n_s = 2.23$), the minimum penetration depth is also lower than $\lambda/100$. This could enable practical imaging schemes in highly absorbing media, with exquisite longitudinal resolution.

VIII. VERIFICATION OF ANALYTICAL MODELS

To validate our analytical models, we compare them with full numerical simulations. For that, we calculate the transfer function of the hyperprism using a full-wave three-dimensional (3D) finite integral method simulation (CST) and compare results with the transfer function obtained from the Fabry-Pérot resonator model. The hyperprism considered in the full-wave simulation is composed of 17×9 silver wires in a square array, embedded in a host dielectric with refractive index n. The diameter and spacing between the wires are $1/80$ and $1/16$ times the width of the hyperprism ($2w = 800$ μm), respectively. The permittivity of the silver is calculated using CST's 2014 model, which relies on a Drude model fitted to experimental data [46]. Owing to the one plane of symmetry of the structure, a half slice of the full structure is considered in the simulation, with perfect magnetic boundary conditions applied in the xz plane [Fig. 1(b)]. In the simulation, a single aperture of size d (the same size as the center-to-center distance between slits) is used as a source field, which is then excited by an x-polarized plane wave propagating along the direction of wires. We evaluate the transfer kernel of the prism from the ratio of the output field to the input field. The output field is calculated on the magnifying side of the prism, and the input field is calculated immediately after the aperture (without the prism). The output field is zero padded outside the location of the imaged aperture. Since the fields (i.e., output and input fields) are in real space, the transfer function obtained is also in real space. In order to obtain the transfer kernel in the spatial Fourier domain, we apply the Fourier transform.

The results obtained from the full-wave simulation and the Fabry-Pérot resonator model are summarized in Fig. 9. The amplitude of the transfer kernel is plotted as a function of normalized wavelength λ/d and wave vector k_u/k_0, and we evaluate the transfer kernel for wires in a dielectric with $n = 1$ and $n = 1.52$. The amplitude of the transfer kernel calculated from the numerical simulation is shown in Figs. 9(a) and 9(c). One can clearly see that the central part of the transmission is shifted [Fig. 9(a)], which is due to the slope of the interface, and greater shift of the central part is observed for $n = 1.52$ [Fig. 9(c)], as expected from Eq. (4). The analytical result is shown in Figs. 9(b) and 9(d), showing good agreement with the simulations in that the shift and the width of the transmission are very similar to the simulation results. Note that in the analytical models we use reflectivity $R = 0.2$, chosen to match the simulated results. At such a low reflectivity,

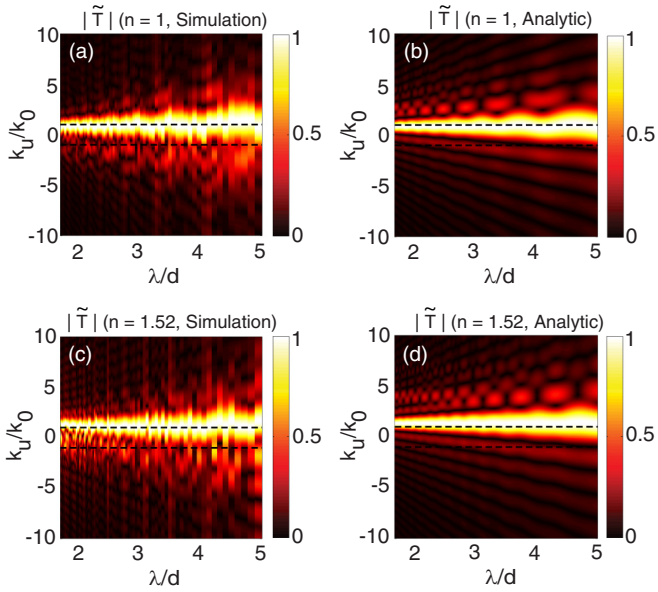

FIG. 9. Calculated transfer kernel of the hyperprism, normalized at each wavelength using (a) and (c) the full-wave 3D simulation and (b) and (d) the Fabry-Pérot resonator model. In the analytical modeling the reflectivity is $R = 0.2$.

the additional grating orders due to the resonance-induced effective grating are barely visible directly. The checkerboard pattern above the main lobes in Figs. 9(b) and 9(d) results from the interference of the sinclike diffraction sidelobes of the specular grating order (due to the finite width) with the first grating diffraction order. There are features suggestive of this checkerboard pattern that also appear in the direct simulations, but noise from the limited spatial resolution of the simulation makes positive identification of this feature difficult.

IX. CONCLUSION

We presented a simple analytic model to calculate the far-field distribution from the near-field excitation of a hyperprism, taking into account resonances. Each wire of the hyperprism acts as a Fabry-Pérot resonator, so that each segment of the hyperprism has resonant frequencies that scale with the coordinate along the base. Remarkably, in the homogenized limit (that is, in the limit of the distance between wires going to zero) this leads to a transmission function identical to that of a grating, but with an effective grating period proportional to the wavelength. The transmission function then becomes that of a nondispersive grating, where the angle between incoming and outgoing orders is shifted by a constant given by geometry rather than wavelength.

As expected, the hyperprism can couple high spatial frequencies to propagating modes. The highest accessible spatial frequencies depend on the slope of the prism and the host refractive index and can by far exceed the spatial frequencies accessible to dielectric prisms.

Our initial motivation was to explore the hyperprism as a (one-dimensional) subdiffraction imaging device. We found that diffraction beating imaging is indeed possible if the background index of the wire medium is air. The wire's resonances scramble the images as we expected, with strong frequency-dependent artifacts, but we showed that an appropriate space-dependent convolution can recover the images over a broad frequency band. However, for larger, more realistic values of the background refractive index, the prism cuts out negative and low spatial frequencies, which makes image reconstruction impossible. Since at higher frequencies such as THz and beyond, it is impractical to realize an air-based hyperprism, hyperprisms have limited potential as practical imaging devices by themselves.

However, the hyperprism offers a new route for selective and tunable excitation of high-k modes from the far-field zone, using a mechanism that is neither conventional refraction nor a grating effect. This offers several new applications. As examples, we discussed how a hyperprism with a large prism angle could be used to excite high-k THz surface modes in graphene and how a hyperprism could enable total internal reflection microscopy with longitudinal resolutions as low as $\lambda/100$. While our analysis relies on the canalization regime, other implementations of the hyperprism should provide similar functionality, with similar limitations. We believe that this could open a new pathway for new experimental approaches for low-frequency plasmonic systems and total internal reflection tomography.

ACKNOWLEDGMENTS

This research was supported by the Australian Research Council (ARC) under Discovery Project scheme number DP120103942 and partly under the ARC Centre of Excellence scheme CUDOS (CE110001018). A.S. acknowledges the Marie Sklodowska-Curie grant of the European Union's Horizon 2020 research and innovation program (Grant No. 708860). S.A. acknowledges the support of ARC funding Grant No. DE140100614. M. S. H. acknowledges a financial support of Australian Postgraduate Award (APA).

[1] D. R. Smith, W. J. Padilla, D. C. Vier, S. C. Nemat-Nasser, and S. Schultz, Phys. Rev. Lett. **84**, 4184 (2000).

[2] A. Poddubny, I. Iorsh, P. Belov, and Y. Kivshar, Nat. Photon. **7**, 948 (2013).

[3] D. R. Smith and D. Schurig, Phys. Rev. Lett. **90**, 077405 (2003).

[4] W. Cai and V. M. Shalaev, *Optical Metamaterials*, Optical Metamaterials: Fundamentals and Applications Vol. 10 (Springer, New York, 2010).

[5] Z. Liu, H. Lee, Y. Xiong, C. Sun, and X. Zhang, Science **315**, 1686 (2007).

[6] P. A. Belov, Y. Hao, and S. Sudhakaran, Phys. Rev. B **73**, 033108 (2006).

[7] R. A. Shelby, D. R. Smith, and S. Schultz, Science **292**, 77 (2001).

[8] A. J. Hoffman, L. Alekseyev, S. S. Howard, K. J. Franz, D. Wasserman, V. A. Podolskiy, E. E. Narimanov, D. L. Sivco, and C. Gmachl, Nat. Mater. **6**, 946 (2007).

[9] Z. Jacob, I. I. Smolyaninov, and E. E. Narimanov, Appl. Phys. Lett. **100**, 181105 (2012).
[10] C. A. Valagiannopoulos, M. S. Mirmoosa, I. S. Nefedov, S. A. Tretyakov, and C. R. Simovski, J. Appl. Phys. **116**, 163106 (2014).
[11] L. Ferrari, D. Lu, D. Lepage, and Z. Liu, Opt. Express **22**, 4301 (2014).
[12] T. Galfsky, H. Krishnamoorthy, W. Newman, E. Narimanov, Z. Jacob, and V. Menon, Optica **2**, 62 (2015).
[13] I. I. Smolyaninov and E. E. Narimanov, Phys. Rev. Lett. **105**, 067402 (2010).
[14] I. I. Smolyaninov, Y.-J. Hung, and E. Hwang, Phys. Lett. A **376**, 2575 (2012).
[15] O. Hess, J. B. Pendry, S. A. Maier, R. F. Oulton, J. Hamm, and K. Tsakmakidis, Nat. Mater. **11**, 573 (2012).
[16] X. Yang, J. Yao, J. Rho, X. Yin, and X. Zhang, Nat. Photon. **6**, 450 (2012).
[17] Z. Jacob, L. V. Alekseyev, and E. Narimanov, Opt. Express **14**, 8247 (2006).
[18] A. Salandrino and N. Engheta, Phys. Rev. B **74**, 075103 (2006).
[19] F. Peragut, L. Cerruti, A. Baranov, J. Hugonin, T. Taliercio, Y. De Wilde, and J. Greffet, Optica **4**, 1409 (2017).
[20] E. Kretschmann and H. Raether, Zeitschrift für Naturforschung. A **23**, 2135 (1968).
[21] I. Avrutsky, I. Salakhutdinov, J. Elser, and V. Podolskiy, Phys. Rev. B **75**, 241402(R) (2007).
[22] Z. Shi, G. Piredda, A. C. Liapis, M. A. Nelson, L. Novotny, and R. W. Boyd, Opt. Lett. **34**, 3535 (2009).
[23] R. W. Wood, Philos. Mag. **4**, 396 (1902).
[24] A. Hessel and A. A. Oliner, Appl. Opt. **4**, 1275 (1965).
[25] M. Kim, S. So, K. Yao, Y. Liu, and J. Rho, Sci. Rep. **6**, 38645 (2016).
[26] J. Rho, Z. Ye, Y. Xiong, X. Yin, Z. Liu, H. Choi, G. Bartal, and X. Zhang, Nat. Commun. **1**, 143 (2010).
[27] G. Shvets, S. Trendafilov, J. B. Pendry, and A. Sarychev, Phys. Rev. Lett. **99**, 053903 (2007).
[28] P. A. Belov, G. K. Palikaras, Y. Zhao, A. Rahman, C. R. Simovski, Y. Hao, and C. Parini, Appl. Phys. Lett. **97**, 191905 (2010).
[29] A. Tuniz, K. J. Kaltenecker, B. M. Fischer, M. Walther, S. C. Fleming, A. Argyros, and B. T. Kuhlmey, Nat. Commun. **4**, 2706 (2013).
[30] J. G. Hayashi, A. Stefani, S. Antipov, R. Lwin, S. D. Jackson, D. D. Hudson, S. Fleming, A. Argyros, and B. T. Kuhlmey, Opt. Express **27**, 21420 (2019).
[31] Y. Zhao, G. Palikaras, P. A. Belov, R. F. Dubrovka, C. R. Simovski, Y. Hao, and C. G. Parini, New J. Phys. **12**, 103045 (2010).
[32] M. S. Habib, A. Stefani, S. Atakaramians, S. C. Fleming, A. Argyros, and B. T. Kuhlmey, Appl. Phys. Lett. **110**, 101106 (2017).
[33] P. A. Belov, C. R. Simovski, and P. Ikonen, Phys. Rev. B **71**, 193105 (2005).
[34] F. L. Pedrotti and L. S. Pedrotti, *Introduction to Optics* (Prentice Hall, Englewood Cliffs, NJ, 1993).
[35] E. G. Loewen and E. Popov, *Diffraction Gratings and Applications* (CRC Press, Boca Raton, FL, 1997).
[36] A. Bitzer, M. Walther, A. Kern, S. Gorenflo, and H. Helm, Appl. Phys. Lett. **90**, 071112 (2007).
[37] S. Pendharker, S. Shende, W. Newman, S. Ogg, N. Nazemifard, and Z. Jacob, Opt. Lett. **41**, 5499 (2016).
[38] A. N. Grigorenko, M. Polini, and K. S. Novoselov, Nat. Photon. **6**, 749 (2012).
[39] M. Jablan, H. Buljan, and M. Soljačić, Phys. Rev. B **80**, 245435 (2009).
[40] S. S. Xiao, X. L. Zhu, B. H. Li, and N. A. Mortensen, Front. Phys. **11**, 117801 (2016).
[41] B. Yao, Y. Liu, S.-W. Huang, C. Choi, Z. Xie, J. F. Flores, Y. Wu, M. Yu, D.-L. Kwong, Y. Huang, Y. Rao, X. Duan, and C. W. Wong, Nat. Photon. **12**, 22 (2018).
[42] X. D. Liu, E. P. J. Parrott, B. S. Y. Ung, and E. Pickwell-MacPherson, APL Photonics **1**, 076103 (2016).
[43] X. D. Liu, Z. F. Chen, E. P. J. Parrott, B. S. Y. Ung, J. B. Xu, and E. Pickwell-MacPherson, Adv. Opt. Mater. **5**, 1600697 (2017).
[44] J. Boulanger, C. Gueudry, D. Munch, B. Cinquin, P. Paul-Gilloteaux, S. Bardin, C. Guerin, F. Senger, L. Blanchoin, and J. Salamero, Proc. Natl. Acad. Sci. USA **111**, 17164 (2014).
[45] A. Wojdyla and G. Gallot, Opt. Lett. **38**, 112 (2013).
[46] P. B. Johnson and R.-W. Christy, Phys. Rev. B **6**, 4370 (1972).